Concurrent role of metal (Sn, Zn) and N species in enhancing the photocatalytic activity of TiO2 under solar light

Concurrent role of metal (Sn, Zn) and N species in enhancing the photocatalytic activity of TiO_2 under solar light

Luca Rimoldi[a,b,*], Eleonora Pargoletti[a,b,*], Daniela Meroni[a,b,*], Ermelinda Falletta[a], Giuseppina Cerrato[c], Francesca Turco[c], Giuseppe Cappelletti[a,b]

[a] *Dipartimento di Chimica, Università degli Studi di Milano, Via Golgi 19, 20133 Milano, Italy*

[b] *Consorzio Interuniversitario Nazionale per la Scienza e la Tecnologia dei Materiali (INSTM), Via Giusti 9, 50121 Firenze, Italy*

[c] *Dipartimento di Chimica and NIS, Inter-departmental Center, Università di Torino, Via Giuria 7, 10125 Torino, Italy.*

[*]*Corresponding authors:* luca.rimoldi@unimi.it; eleonora.pargoletti@unimi.it; daniela.meroni@unimi.it

Abstract

TiO_2 modification by both non-metal and metal species is a popular strategy to promote the semiconductor visible light absorption and photocatalytic performance. In this work, tin and zinc are compared as metal promoters to enhance the photocatalytic activity of N-doped TiO_2 under solar light. The synthesized samples were tested under both UV and simulated solar irradiation toward the photocatalytic degradation of tetracycline, an emerging water pollutant. All copromoted samples (N+Sn and N+Zn) revealed higher efficiency under solar light in the mineralization of the pollutant with respect to both the pristine and N-doped ones. The enhanced photocatalytic efficiency of these samples was traced back to the modifications introduced by the different guest species to the structural (X-ray Powder Diffraction, XRPD), morphological (High-Resolution Transmission Electron Microscopy, HR-TEM and Brunauer-Emmett-Teller analysis, BET), spectroscopic (X-ray Photoelectron Spectroscopy, XPS, Energy Dispersive X-ray Spectroscopy,

EDX and Diffuse Reflectance Spectroscopy, DRS) and surface features (ζ-potential). In this regard, the increased surface area, the modifications of the phase composition and the enhanced visible light harvesting seem to play a pivotal role in affecting the photocatalytic performance. Mass spectrometry analyses allowed us to identify several reaction intermediates and propose different degradation mechanisms depending on the type of metal promoter.

Keywords

N-doped TiO_2 photocatalyst; Sn/Zn guest species; tetracycline; ESI-MS; photodegradation pathways; ζ-potential.

1. Introduction

Titanium dioxide (TiO_2) is probably the most widely adopted photocatalyst, due to its chemical and thermal stability, low cost, non-toxicity and high efficiency under UV irradiation. However, its wide band gap (≥ 3.0 eV) prevents the use of visible light to activate the semiconductor. Non-metal species have been extensively adopted in order to enhance its visible light harvesting. Among these elements, starting from the pioneering work of Asahi *et al.* [1], nitrogen has been the focus of extensive research as it proved able to promote visible light absorption. Nonetheless, the introduction of N as guest species in the TiO_2 lattice generates localized intra gap states that can promote electron/hole recombination phenomena, thus decreasing the photocatalytic efficiency [2].

A viable strategy to improve the photocatalytic activity of N-doped TiO_2 is the development of mixed oxide structures and heterojunctions able to limit recombination phenomena by enhancing the charge separation [3,4]. Due to their band structure, SnO_2 and ZnO have been frequently adopted to develop SnO_2/TiO_2 and ZnO/TiO_2 heterojunctions [5–12], although reports of the formation of heterojunctions with N-doped TiO_2 have been much more scarce.

Codoping of TiO_2 with nitrogen and a metal species has also emerged as a promising strategy to boost the photocatalytic efficiency of N-doped materials. Several transition elements have been reported as efficient codopants of N-doped TiO_2 [13–15], leading in some cases to synergistic effects in the visible light absorption [16,17]. Few articles can be found in the literature regarding codoping of TiO_2 with N and Zn or Sn [18]. Zhuang *et al.* reported an enhanced activity of Sn and N-codoped TiO_2 systems with respect to both photocatalytic hydrogen evolution and Rhodamine B degradation [19]. Kaur *et al.*, studying a series of metal,N codoped titania systems, suggested Zn as an efficient species able to promote photocatalysis reducing the recombination centres [20]. The improved photocatalytic activity of Zn,N-codoped TiO_2 was confirmed by Hu *et al.* for samples prepared by nitridation and hydrogenation with high oxygen vacancies content [21].

In the present work, the modifications provided by Sn and Zn species on the physicochemical features and the photocatalytic activity of N-doped TiO_2 systems was studied. High metal contents

were investigated to favour the occurrence of partial segregation of the metal oxides. The obtained samples were characterized from the structural, morphological, optical and spectroscopic point of view. Their photocatalytic activity was tested both under UV and simulated solar irradiation toward the degradation of tetracycline (TC), an emerging organic pollutant belonging to the class of pharmaceutics and personal care products (PPCPs). To the authors' best knowledge, for the first time, differences in the photocatalytic degradation mechanism of Sn- and Zn-modified titania samples were identified and related to the modifications of the physicochemical features induced by metal species.

2. Experimental section

2.1. Sample preparation

Reactants were purchased from Sigma-Aldrich and used without further purification. Solutions and suspensions were prepared with doubly-distilled water, passed through a Milli-Q apparatus.

In a typical synthesis, carried out at 60 °C, 10.7 g of titanium(IV) isopropoxide and 11.3 g of 2-propanol were mixed for 15 min. In the case of the metal modified samples, the required amount of $SnCl_4 \cdot 5H_2O$ or $ZnCl_2$ was dissolved in the mixture. Successively, 65 mL of either NH_4OH (N/Ti molar ratio = 0.5) or KOH aqueous solution for N-doped and undoped samples, respectively, was added drop-by-drop while stirring vigorously (300 rpm). In both cases, the base solution concentration was adjusted in order to obtain a final pH of 9. The reaction mixture was then stirred for 90 min to complete the hydrolysis. The resulting precipitate was washed three times by centrifugation-resuspension cycles and later dried at 80 °C overnight. Finally, the xerogel was calcined at 400 °C for 6 h under oxygen flux (9 NL h^{-1}). TiO_2 samples were labelled as Ti, TiN, TiNSnx, and TiNZnx for undoped, N-doped and N,metal co-promoted samples, respectively, where *x* identifies the metal/Ti molar ratio (5 or 20%).

2.2. Materials characterization

The adopted material characterizations are detailed in the Supplementary Material.

2.3. Photocatalytic tests

All samples were tested toward the photocatalytic degradation of tetracycline hydrochloride in water under both UV (Jelosil HG500 lamp; effective irradiation power: 30 mW cm^{-2}) and simulated solar light (Lot Oriel halogen lamp; effective irradiation power: 7.5 mW cm^{-2}) irradiation. Photocatalytic experiments were performed at 20 °C in a 300-mL jacketed reactor using an initial TC concentration of 35 mg L^{-1} and a photocatalyst concentration of 0.5 g L^{-1}. An oxygen flux (9 NL h^{-1}) was bubbled in the reactor during the photocatalytic experiments. Both the TC disappearance and the mineralization degree were monitored as described previously [22]. Before light irradiation, samples were left in the dark for 30 min in order to reach the adsorption equilibrium. Photolysis tests were also conducted to quantify the molecule degradation in the absence of photocatalyst, leading to less than 5% mineralization. Initial kinetic constants (pseudo-first order) were calculated within 35 min and 120 min of irradiation in the case of UV and solar irradiation, respectively.

The reaction intermediates were also investigated by electrospray ionization mass spectrometry (ESI-MS) using a LCQ Advantage system (Thermo Finnigan) MS spectrometer, equipped with an electrospray ionization source and an 'Ion Trap' mass analyser. Sample solutions were analyzed by direct infusion, applying +3.0 kV at the capillary entrance and using a drying gas at 350°C. Full-scan MS spectra were acquired in the 150–1000 mass/charge (*m/z*) range.

3. Results and discussion

3.1. Materials characterization

Fig. 1 reports the XRPD patterns of the investigated samples. Sharp differences in terms of phase composition and average crystallite size are appreciable depending on the nature and nominal amount of the guest species (Tab. 1). The undoped sample is an anatase-brookite composite in a *ca.* 2:1 ratio, as clearly appreciable from the presence of the brookite (121) reflection. N-doping promotes the anatase content (space group: $I4_1/amd$; tetragonal structure) and crystal growth (Tab. 1), in agreement with previous reports about N-doped TiO_2 [23,24].

The presence of Sn seems instead to result in lower crystallinity and anatase content with respect to TiN sample. In particular, TiNSn5 showed *ca.* 22% of brookite (space group: *Pbca*; orthorhombic structure) and smaller crystallites, whereas the higher Sn content promotes the rutile phase (space group: $P4_2/mnm$; tetragonal structure), which is the only phase clearly appreciable. These phenomena can be explained on the grounds of the structural similarity of rutile TiO_2 and SnO_2-cassiterite (space group: $P4_2/mnm$; tetragonal structure), which can favour the growth of rutile at low temperatures (< 500 – 600 °C). Interestingly, XRPD analyses show no well-defined peaks related to SnO_2 segregated phases.

Zn-promoted samples show a marked decrease in crystallinity, which is already clear from the XRPD pattern of TiNZn5 (Fig. 1). This phenomenon can be rationalized considering the sharp difference among the crystalline habits of TiO_2 polymorphs and ZnO wurtzite (the most likely ZnO polymorph to form in the adopted synthetic conditions, space group: $P6_3mc$; hexagonal structure), which might inhibit the TiO_2 crystal growth in the presence of Zn species. As in the case of Sn-modified samples, no well-defined peaks related to segregated phases (ZnO polymorphs) are appreciable from XRPD patterns, even at the highest Zn content (Fig. 1).

The structural modification in terms of anatase cell distortion is highlighted by the shift of the anatase (101) diffraction peak towards lower 2θ values for both N- and metal-modified samples with respect to the pristine Ti material (Fig. S1). A shift of 0.05° was recorded in the case of N- and N,Zn-modified samples, with respect to the pristine material. A distortion of the anatase cell was previously reported by Lo Presti and co-authors [23] in the case of N-doped samples. A more marked shift (0.1°) was recorded in the case of TNSn5. It is worth noting that the TiNSn20 sample shows a phase transition to rutile.

These results suggest a higher affinity of Sn species for the titania lattice with respect to the Zn species, due to either the same oxidation state of Ti or its tendency to form the same tetragonal polymorphic structure. Differently, the presence of Zn, characterized by lower valence and its growth in hexagonal wurtzite, mostly decreases the sample crystallinity.

In order to corroborate XRPD outcomes, XPS spectra were acquired. All samples show the presence of Ti(IV) (Fig. 2, Ti $2p_{3/2}$ and Ti $2p_{1/2}$ peaks at 458.5 and 464.0 eV, respectively), while Sn(IV) (3d region at 486.1 and 494.8 eV) and Zn(II) (2p region at 1021.5 and 1044.0 eV) peaks were detected in metal-modified samples (Fig. S2). Slightly higher Sn/Zn contents with respect to the nominal amounts were measured by XPS, possibly indicating the occurrence of surface segregation phenomena of metal guest species. On the other hand, Sn/Ti and Zn/Ti molar ratios, retrieved by EDX analyses, are comparable to the theoretical amount, within experimental error, for all metal-modified samples. It should be noted that EDX analyses have a local character and results might not be indicative of the whole sample elemental composition. Furthermore, in the case of Sn- and Zn-modified samples, peak components ascribable to Ti(IV+δ) species (459.1 and 464.8 eV) were appreciable [25]. The Ti(IV+δ)/Ti(IV) ratios (*ca.* 0.4 and 0.7 for TiNSn5 and TiNZn5, respectively) support a higher surface defectivity in the case of Zn-modified systems (Fig. 2). The O 1s region (Fig. S3) exhibits for all samples a multi-component signal, presenting a main peak at around 529.6 eV (peak I in Fig. S3a), attributable to lattice O species, and two minor components centred at ~ 530.8 eV (peak II in Fig. S3a) and ~ 532.0 eV (peak III in Fig. S3a), which can be related to surface hydroxyls and chemisorbed oxygen species, respectively [26,27]. While no significant differences in the O 1s peak positions were appreciable, the relative intensities of peak components markedly vary among the samples. In particular, the components at higher B.E. were significantly more intense in the metal-modified samples with respect to Ti and TiN, also supporting a higher defectivity of these samples.

Fig. 3 reports HR-TEM micrographs of bare and promoted TiO_2. Both Ti and TiN samples (Fig. 3a,b) show pseudo-spherical crystallites with a good degree of crystallinity and interplanar distances characteristics of anatase TiO_2 (d_{101} = 0.339 – 0.342 nm), in good agreement with XRPD findings. The TiNSn5 sample shows crystalline particles (3 – 6 nm) in which both anatase (d_{101} = 0.339 – 0.342 nm; inset of Fig.3c) and brookite (d_{211} = 0.291 – 0.294 nm) interplanar distances are

recognizable (Fig. 3c). However, with respect to XRPD results, a small content of SnO_2 cassiterite (d_{111} = 0.223 – 0.227 nm; inset of Fig. 3c) is appreciable. In the case of TiNSn20 (Fig. 3d), crystalline particles with a broader size distribution (showing also particles over 10 nm) are appreciable. Interplanar distances reveal the presence of rutile (d_{101} = 0.246 – 0.249 nm; inset of Fig. 3d), as well as of SnO_2 cassiterite (d_{101} = 0.260 – 0.263 nm; inset of Fig. 3d). The addition of Zn leads to a broader size distribution and poorer sample crystallinity (Fig. 3e,f), as well as to a higher amorphous content, in agreement with XRPD findings. However, also in the case of Zn, HR-TEM analyses show the presence of a guest oxide phase (ZnO wurtzite, d_{101} = 0.290 – 0.293 nm), which was not detected by XRPD, possibly due to both the low amount and the oxide preferential segregation at the photocatalyst surface.

N_2 adsorption-desorption isotherms under subcritical conditions (T = – 196 °C) of all samples are characteristic of mesoporous materials (Fig. S4). While the undoped sample presents an H2-type hysteresis loop with high total porosity (Tab. 1, Fig. S4), N-doping sharply decreases the total porosity for all the sensitized samples (Tab. 1). In this regard, all the prepared powders exhibit invariably a notable decrease of the average pore size with respect to the pristine TiO_2 (Fig. S5), as well as a drop in the total pore volume (Tab. 1), when either N or metal species are introduced. The sole N-doping also leads to a notable decrease in surface area with respect to the undoped reference (Tab. 1), as a result of lower total porosity and larger crystallites. On the other hand, metal addition invariably resulted in larger surface areas, more so in the case of Zn-modified samples, as expected on the grounds of their higher amorphous content. The higher specific surface area of Zn-modified samples might favour a TC degradation pathway involving a direct attack of photogenerated holes to the adsorbed pollutant molecule.

Moreover, the photocatalyst surface features were characterized by ζ-potential measurements performed at the pH conditions of photocatalytic tests (pH *ca.* 4). All samples show a positive value of the ζ-potential, *i.e.* a positive surface charge. The highest values were found for the pristine and the N-doped samples, while the introduction of the metal species decreases the surface charge of the

material, more so in the case of Sn and of higher metal content (Tab. 1). The lower surface charge of metal-modified samples might favour the adsorption of TC, due to its partial speciation as positively charged species at the photocatalytic test conditions [28].

DRS spectra revealed the typical sigmoidal shape for undoped TiO_2 (Fig. 4). Band gap values of the prepared materials were evaluated by applying the Kubelka-Munk elaboration. The band gap of the Ti sample was determined to be 3.26 eV, as expected on the grounds of its phase composition (anatase and brookite have a reported band gap of 3.2 and *ca.* 3.3 eV, respectively [29,30]). N-doping led to a localized light absorption in the visible region in the 400 – 550 nm range, which resulted in a slight decrease of the apparent band gap (3.22 eV). This absorption has been previously reported in the case of N-doped samples [29,31–34] and attributed to mid-gap states introduced by interstitial nitrogen [2], often related to enhanced recombination effects.

Sn- and Zn-modified samples show different behaviours in terms of light absorption (Fig. 4 and S6). Sn-modified samples behave similarly to N-doped TiO_2. With respect to the latter, however, Sn-modified samples present a slight redshift of the absorption edge and a more marked absorption in the 400 – 600 nm range (Fig. 4a and S6a). Both effects are more appreciable increasing the Sn content. A similar effect was reported in the case of Nb,N-codoped samples [16,17] and attributed to charge compensation phenomena taking place between the two guest species. In the case of the Sn-promoted samples, the observed visible sensitization cannot be explained by the presence of segregated oxide, due to the large band gap of SnO_2 (3.6 eV). It is therefore indicative of the formation of intragap states as a consequence of the introduction of defects/heteroatoms in the TiO_2 lattice. Zn-promoted samples show a redshift of the absorption edge as well, resulting in a decrease of the apparent band gap (Tab. 1). However, the N-doping characteristic absorption in the visible region is less appreciable in these samples and does not vary with the Zn-content (Fig. 4b and S6b). This effect might be indicative of a lower N content introduced in the TiO_2 lattice, due to the lower crystallinity and higher amorphous content of Zn-modified samples.

3.2. Photocatalytic tests

The prepared photocatalysts were tested toward the degradation of an emerging water pollutant, tetracycline, under both UV and simulated solar light irradiation. A photocatalytic time of 3 h was selected to obtain an almost complete disappearance of the TC molecule (Tab. S1) for all the tested photocatalysts under UV light in the adopted experimental conditions (Fig. S7a). Initial kinetic constants under UV irradiation (Tab. S1) revealed the most performing photocatalyst to be Ti, while guests introduction resulted in a decrease of the molecule degradation rate, in particular for metal (Sn and Zn)-modified samples (Fig. S7a). Undoped Ti shows a higher TC disappearance kinetic constant also with respect to TiN, in agreement with its larger surface area. Fig. 5 compares the mineralization degrees of the synthesized samples at the end of the photocatalytic tests. An incomplete mineralization is observed in all cases, even under UV irradiation, reaching the highest value (73%) for the Ti sample. The undoped Ti and TiN present a fully comparable mineralization degree due to the balancing of morphological and structural effects: on one side, the undoped Ti sample presents a higher surface area, while TiN shows a higher content in anatase, often regarded as the most active TiO_2 crystal phase. These two effects can partly balance off and lead to comparable mineralization degrees for the two samples under a high intensity UV light (*i.e.*, in favourable reaction conditions). The mineralization trend under UV irradiation (Fig. 5) shows invariably a worse performance for metal-modified samples with respect to Ti and TiN, more so for Zn-doped photocatalysts and in the case of the highest metal content (guest metal/Ti molar ratio of 20%).

The scenario is completely different for photocatalytic tests performed under simulated solar light irradiation. As expected on the grounds of the lower effective power density and broader wavelength range, a slower TC disappearance is appreciable under simulated solar irradiation than under UV light (Tab. S1) leading to an incomplete molecule disappearance in the investigated reaction time (Tab. S1, 4^{th} column and Fig. S7b) and lower mineralization degrees (Fig. 5) are observed with respect to UV tests. Furthermore, all the metal-modified samples present higher mineralization with respect to the undoped and N-doped samples (Fig. 5). TiNSn5 showed the best

overall performance. The TiNZn20 sample presents a similar mineralization degree with respect to TiNSn5, even though the kinetic constant (Tab. S1, 5th column) is far lower, suggesting differences in the reaction pathways between the two samples. With respect to N-doped TiO_2, whose visible light absorption does not result in an improved visible light activity, Sn,N- and Zn,N-copromoted samples show a synergistic effect in terms of both visible light absorption and photocatalytic activity, as also reported in previous literature reports [19–21].

On the grounds of these results, the tetracycline photocatalytic degradation mechanisms reported in Fig. S8 can be proposed in the case of pure, N-doped and metal-modified samples, after 35 minutes of UV irradiation. The reported by-products have been identified by evaluating the *m/z* values from MS spectra (Fig. S9). Starting from the pristine TC molecule ($[TC+H]^+$, *m/z* 445) and its relative Na-adduct ($[TC+Na]^+$, *m/z* 467, Fig. S1), two diverse attacks could be hypothesized, mediated by either OH radicals (route a) or photogenerated holes, h^+ (route b), on the grounds of literature results [35–37]. In the former, the degradation may imply several steps consisting in dehydroxylations, loss of the $–N(CH_3)_2$ group and formation of a carboxylic termination eventually leading to product A ($[A+H]^+$, *m/z* 371) [38]. Then, a ring opening occurs ($[B+H]^+$, *m/z* 297) followed by oxidation reactions and the loss of the methyl group ($[C+H]^+$, *m/z* 242). This latter compound was identified by Niu *et al.* in the case of tetracycline photodegradation by TiO_2 [35]. Further degradation products, with *m/z* 203 and 172 ($[D+H]^+$ and $[E+H]^+$, respectively) come from the progressive breakage of the aromatic rings [39]. MS analyses were carried out also after longer irradiation time (65 min) and a representative example is reported in Fig. S10. With respect to the relative spectrum at 35 min, the same main peaks are appreciable although with different relative intensities. In particular, the peaks associated with the TC molecule ($[TC+H]^+$, *m/z* 445, and the Na-adduct $[TC+Na]^+$, *m/z* 467) markedly decrease in intensity, in agreement with the kinetic and mineralization data. Route b, on the contrary, assumes the dealkylation of the tertiary amine ($[F+H]^+$, *m/z* 417) [35], the subsequent loss of $–NH_2$ and the reduction of the amide group to a

ketone moiety ($[G+H]^+$, *m/z* 301). Nevertheless, no other lower molecular weight intermediates can be detected.

By detecting these intermediates in the MS spectra (Fig. S9), Ti, TiN, and TiNSn20 seem to follow path a, whereas with the Zn-modified sample (TiNZn20), route b has to be preferred. In the latter case, the formation of F and G by-products might hinder any further oxidation steps: actually, TiNZn20 shows lower photocatalytic performance (Tab. S1) and mineralization degree (see Fig. 5).

In the case of solar light tests, the data concerning 3 h reaction time were selected and presented here as the most significant for comparison, due to the lower degradation rate with respect to UV irradiation. In this case, the lower signal to noise ratios in the case of the metal-modified samples with respect to the pristine Ti sample indicates the presence of a lower amount of by-products, due to their higher photocatalytic efficiency under solar light with respect to the undoped sample (Fig. S11). Moreover, lighter by-products ($[I+H]^+$ and $[L+H]^+$ species, Fig. S2) have also been detected ascribable to both pathways (Fig. S11). While the pristine and Sn-promoted samples exhibit the same main degradation intermediates under both UV and similar solar irradiation (see *e.g.*, the peaks at *m/z* 371 and 297 in Figs. S9 and S11), Zn,N-modified samples exhibit different by-products in the two series of tests. Hence, we cannot exclude that different degradation pathways prevail under simulated solar irradiation. It is noteworthy that both pristine and Sn-promoted samples show a relatively fast TC disappearance but a comparatively lower mineralization degree, whereas Zn-promoted samples despite the slower kinetic constant (Tab. S1) show appreciable mineralization (Fig. 5).

4. Conclusions

In this work, the modifications imparted by Sn and Zn species on the physicochemical properties and photocatalytic activity of N-doped TiO_2 photocatalysts are presented. The metal (Sn, Zn) addition leads to significant variations of the structural, morphological, spectroscopic and surface properties with respect to both the pristine and the N-doped titania.

Metal promoters are present as Sn(IV) and Zn(II) species within the samples, as shown by Sn 3d and Zn 2p XPS spectra. HR-TEM images show the presence of crystalline phases of Sn and Zn oxides. However, despite the high metal contents investigated, no segregated SnO_2/ZnO phases are appreciable from XRPD patterns. Considering the higher surface content of metal species shown by XPS analyses, and the marked change in surface charge shown by ζ-potential measurements, a preferential location of the segregated metal species at the sample surface can be proposed. The addition of both metals leads to a general increase in the TiO_2 defectivity, as appreciable from Ti 2p and O 1s XPS spectra. However, the two metal species seem to have instead two different effects on the TiO_2 lattice. Sn promotes the formation of rutile TiO_2, which can be expected on the grounds of the structural similarity of TiO_2 rutile ($P4_2/mnm$, a = 4.5937 Å, c = 2.9587 Å) and SnO_2 cassiterite ($P4_2/mnm$, a = 4.7382 Å, c = 3.1871 Å). Considering the similar ionic radii of Ti(IV) and Sn(IV) species [40], Sn species could partially substitute Ti in the TiO_2 lattice, as also supported by the observed shift of XRPD peak position for Sn-modified samples (Fig. S1). On the other hand, the introduction of Zn leads mainly to a loss of TiO_2 crystallinity (appreciable in both XRPD patterns and HR-TEM images), which can be rationalized considering the marked structural diversity of ZnO wurtzite ($P6_3mc$; hexagonal structure a = 3.82, c = 6.26) with respect to the main TiO_2 polymorphs. These structural differences might explain the observed electronic features of the two sets of metal-promoted materials: DRS spectra show the formation of intragap states for Sn-promoted samples, possibly due to heteroatoms [19], whereas in the case of Zn-modified samples, the observed optical features (such as, a redshift of the absorption edge) could be related to the increased TiO_2 defectivity [41].

At the investigated metal content, partial segregation of the guest oxides is appreciable only by HR-TEM, while other marked structural changes are observed by XRPD: favoured rutile formation for Sn-modified samples and higher amorphous content for Zn-modified ones. The higher defectivity of metal-modified samples, shown not only by XRPD analyses but also by the relevant changes in the surface properties (XPS and ζ-potential measurements), crucially affects the samples' optical and

electronic features (DRS). Both sets of metal-promoted samples display a redshift of the absorption edge with respect to both pure and N-doped TiO_2, and a light absorption component at longer wavelength which can be attributed to intragap states related to lattice defects. The higher surface defectivity and the lower ζ-potential values with respect to both pristine and N-doped TiO_2, together with the enhanced surface area, can promote TC adsorption and subsequent degradation in the case of the metal-modified photocatalysts. In agreement with previous reports [16,31], the sole N-doping, despite the increased visible light harvesting, fails to enhance the photocatalytic activity under simulated solar irradiation with respect to the pristine sample. This phenomenon has been attributed to favoured recombination pathways of photogenerated charges due to mid-gap states generated by N doping, particular interstitial one [16,31]. The addition of metal species, instead, bestowed enhanced photocatalytic performance in the tetracycline mineralization under simulated solar light with respect to both the pristine and N-doped samples. As the formation of segregated guest oxide phases comes along with the modification of the host lattice, it is complex to single out the effect of a specific photocatalyst feature on its photocatalytic activity. However, the better performance of the metal-modified photocatalysts under simulated sunlight can be related to their optical and electronic features, arising from the higher defectivity with respect to both pure and N-doped samples. Moreover, it is worth noting that, as already reported by other researchers [42,43], the detrimental effect of crystallinity loss, as here observed in particular for Zn-modified samples, can be overcome by a surface area enhancement and a major defectivity of the sample, beneficial for the photocatalytic efficiency under solar or visible light.

The modifications of the physicochemical features induced by metal species also stand at the basis of the differences in the photocatalytic degradation mechanism of Sn- and Zn-modified samples which were identified here for the first time. In particular, the prevalence of a direct attack mechanism in Zn-modified samples was related to their higher surface areas and surface defectivity, arising from the low structural compatibility between ZnO and TiO_2 species.

References

[1] R. Asahi, T. Morikawa, T. Ohwaki, Y. Taga, Science 293 (2001) 269–271.

[2] R. Asahi, T. Morikawa, H. Irie, T. Ohwaki, Chem. Rev. 114 (2014) 9824–9852.

[3] P. V Kamat, J. Phys. Chem. Lett. 3 (2012) 663–672.

[4] G. Liu, L. Wang, H.G. Yang, H.-M. Cheng, G.Q. (Max) Lu, J. Mater. Chem. 20 (2010) 831–843.

[5] X. Li, C. Gao, H. Duan, B. Lu, Y. Wang, L. Chen, Z. Zhang, X. Pan, E. Xie, Small 9 (2013) 2005–2011.

[6] A. Enesca, M. Baneto, D. Perniu, L. Isac, C. Bogatu, A. Duta, Appl. Catal. B Environ. 186 (2016) 69–76.

[7] F. Xie, Y. Li, J. Dou, J. Wu, M. Wei, J. Power Sources 336 (2016) 143–149.

[8] H. Cao, S. Huang, Y. Yu, Y. Yan, Y. Lv, Y. Cao, J. Colloid Interface Sci. 486 (2017) 176–183.

[9] M. Kwiatkowski, R. Chassagnon, O. Heintz, N. Geoffroy, M. Skompska, I. Bezverkhyy, Appl. Catal. B Environ. 204 (2017) 200–208.

[10] L. Lv, X. Bai, Z. Ye, CrystEngComm. 18 (2016) 7580–7589.

[11] E.A. Floriano, L.V.A. Scalvi, M.J. Saeki, J.R. Sambrano, J. Phys. Chem. A 118 (2014) 5857–5865.

[12] R. Wang, H. Tan, Z. Zhao, G. Zhang, L. Song, W. Dong, Z. Sun, J. Mater. Chem. A 2 (2014) 7313.

[13] J.J. Brancho, B.M. Bartlett, Chem. Mater. 27 (2015) 7207–7217.

[14] X. Ma, Y. Wu, Y. Lu, J. Xu, Y. Wang, Y. Zhu, J. Phys. Chem. C 115 (2011) 16963–16969.

[15] Q. Meng, T. Wang, E. Liu, X. Ma, Q. Ge, J. Gong, Phys. Chem. Chem. Phys. 15 (2013) 9549–61.

[16] L. Rimoldi, C. Ambrosi, G. Di Liberto, L. Lo Presti, M. Ceotto, C. Oliva, D. Meroni, S. Cappelli, G. Cappelletti, G. Soliveri, S. Ardizzone, J. Phys. Chem. C 119 (2015) 24104–24115.

[17] C. Marchiori, G. Di Liberto, G. Soliveri, L. Loconte, L. Lo Presti, D. Meroni, M. Ceotto, C. Oliva, S. Cappelli, G. Cappelletti, C. Aieta, S. Ardizzone, J. Phys. Chem. C 118 (2014) 24152–24164.

[18] E. Wang, T. He, L. Zhao, Y. Chen, Y. Cao, J. Mater. Chem. 21 (2011) 144–150.

[19] H. Zhuang, Y. Zhang, Z. Chu, J. Long, X. An, H. Zhang, H. Lin, Z. Zhang, X. Wang, Phys. Chem. Chem. Phys. 18 (2016) 9636–9644.

[20] N. Kaur, S.K. Shahi, V. Singh, Photochem. Photobiol. 92 (2016) 69–75.

[21] Y. Hu, G. Chen, C. Li, Y. Yu, J. Sun, H. Dong, New J. Chem. 39 (2015) 2417–2420.

[22] L. Rimoldi, D. Meroni, G. Cappelletti, S. Ardizzone, Catal. Today 281 (2017) 38–44.

[23] L. Lo Presti, M. Ceotto, F. Spadavecchia, G. Cappelletti, D. Meroni, R.G. Acres, S. Ardizzone, J. Phys. Chem. C 118 (2014) 4797–4807.

[24] M. Ceotto, L. Lo Presti, G. Cappelletti, D. Meroni, F. Spadavecchia, R. Zecca, M. Leoni, P. Scardi, C.L. Bianchi, S. Ardizzone, J. Phys. Chem. C 116 (2012) 1764–1771.

[25] E. Pargoletti, G. Cappelletti, A. Minguzzi, S. Rondinini, M. Leoni, M. Marelli, A. Vertova, J. Power Sources 325 (2016) 116–128.

[26] S. Ardizzone, C.L. Bianchi, D. Tirelli, Colloids Surfaces A Physicochem. Eng. Asp. 134 (1998) 305–312.

[27] L. Jing, B. Xin, F. Yuan, L. Xue, B. Wang, H. Fu, J. Phys. Chem. B 110 (2006) 17860–17865.

[28] M. Brigante, P.C. Schulz, J. Hazard. Mater. 192 (2011) 1597–1608.

[29] V.N. Kuznetsov, N. Serpone, J. Phys. Chem. C 113 (2009) 15110–15123.

[30] A. Di Paola, M. Bellardita, L. Palmisano, Catalysts 3 (2013) 36–73.

[31] D. Meroni, S. Ardizzone, G. Cappelletti, C. Oliva, M. Ceotto, D. Poelman, H. Poelman, Catal. Today 161 (2011) 169–174.

[32] N. Serpone, J. Phys. Chem. B 110 (2006) 24287–24293.

[33] G. Liu, G.Y. Hua, X. Wang, L. Cheng, J. Pan, Q.L. Gao, H.M. Cheng, J. Am. Chem. Soc. 131 (2009) 12868–12869.

[34] S. Livraghi, M.C. Paganini, E. Giamello, A. Selloni, C. Di Valentin, G. Pacchioni, J. Am. Chem. Soc. 128 (2006) 15666–15671.

[35] J. Niu, S. Ding, L. Zhang, J. Zhao, C. Feng, Chemosphere 93 (2013) 1–8.

[36] R.A. Palominos, M.A. Mondaca, A. Giraldo, G. Peñuela, M. Pérez-Moya, H.D. Mansilla, Catal. Today 144 (2009) 100–105.

[37] X.D. Zhu, Y.J. Wang, R.J. Sun, D.M. Zhou, Chemosphere 92 (2013) 925–932.

[38] M. Cao, P. Wang, Y. Ao, C. Wang, J. Hou, J. Qian, J. Colloid Interface Sci. 467 (2016) 129–139.

[39] L. Jinhai, M. Han, Y. Guo, F. Wang, L. Meng, D. Mao, S. Ding, C. Sun, Appl. Catal. A Gen. 524 (2016) 105–114.

[40] J.C. Slater, J. Chem. Phys. 41 (1964) 3199–3204.

[41] V.N. Kuznetsov, V.K. Ryabchuk, A. V. Emeline, R. V. Mikhaylov, A. V. Rudakova, N.

Serpone, Chem. Mater. 25 (2013) 170–177.

[42] Y. Li, T. Sasaki, Y. Shimizu, N. Koshizaki, J. Am. Chem. Soc. 130 (2008) 14755–14762.

[43] D. Zywitzki, H. Jing, H. Tüysüz, C.K. Chan, J. Mater. Chem. A 5 (2017) 10957–10967.

Table 1 – Phase composition (A: anatase, B: brookite, R: rutile) and average crystallite size of the most abundant phase, estimated from XRPD analyses, $<D_v>$; guest/Ti molar ratios determined from EDX analyses; specific surface area, $S_{BET,}$ and total pore volume, V_{pores}; apparent band gap values determined by Kubelka-Munk approach, E_g; ζ-potential values at pH 4.

Sample	**XRPD phase composition / %**	**$<D_v>$ / nm**	**guest/Ti (EDX) / at. %**	**S_{BET} / $m^2\ g^{-1}$**	**V_{pores} / mL g^{-1}**	**E_g / eV**	**ζ-potential / mV**
Ti	66 A – 34 B	6	-	188	0.308	3.26	+ 23.7
TiN	88 A – 12 B	12	-	115	0.096	3.22	+ 26.5
TiNSn5	78 A – 22 B	9	5.8	215	0.079	3.11	+ 14.7
TiNSn20	100 R *	11	26.1	197	0.104	3.12	+ 9.7
TiNZn5	100 A ‡	9	5.7	272	0.087	3.13	+ 18.2
TiNZn20	-	-	19.9	311	0.108	3.17	+ 14.2

* A small amount of anatase cannot be excluded. ‡ Amorphous phase is also appreciable.

Figure captions

Figure 1 – XRPD patterns of the synthesized samples. The main peaks of the three TiO_2 phases (A: anatase, B: brookite, R: rutile) are highlighted.

Figure 2 – XPS spectra of the Ti 2p region for Ti (a), TiN (b), TiNSn5 (c) and TiNZn5 (d).

Figure 3 – HR-TEM images of Ti (a), TiN (b), TiNSn5 (c), TiNSn20 (d), TiNZn5 (e), and TiNZn20 (f). Insets: Fast Fourier Transform (FFT) patterns of the investigated polymorphs.

Figure 4 – Diffuse reflectance spectra for Sn (a) and Zn (b) modified samples.

Figure 5 – Mineralization degrees at the end of the photocatalytic test under UV and simulated solar irradiation.

Figure 1

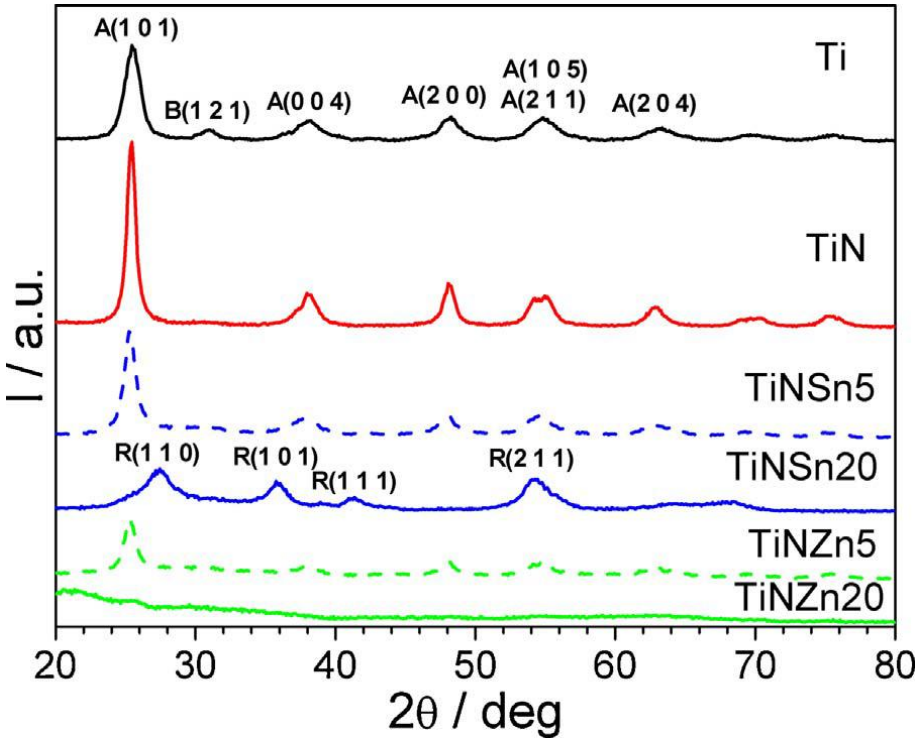

Figure 2

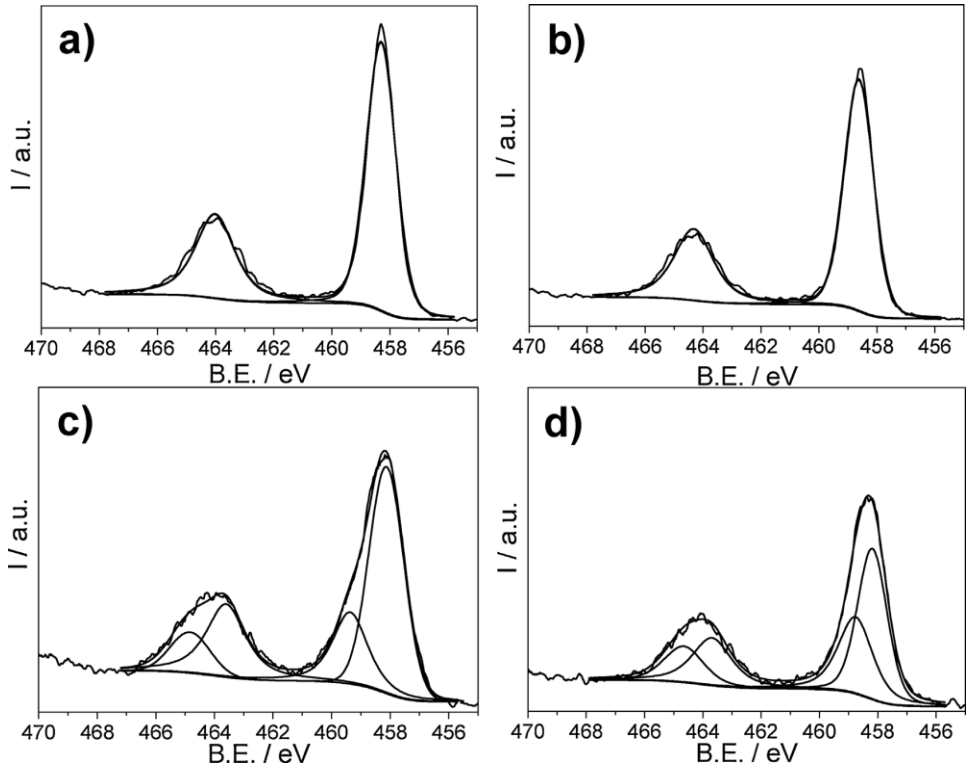

Figure 3

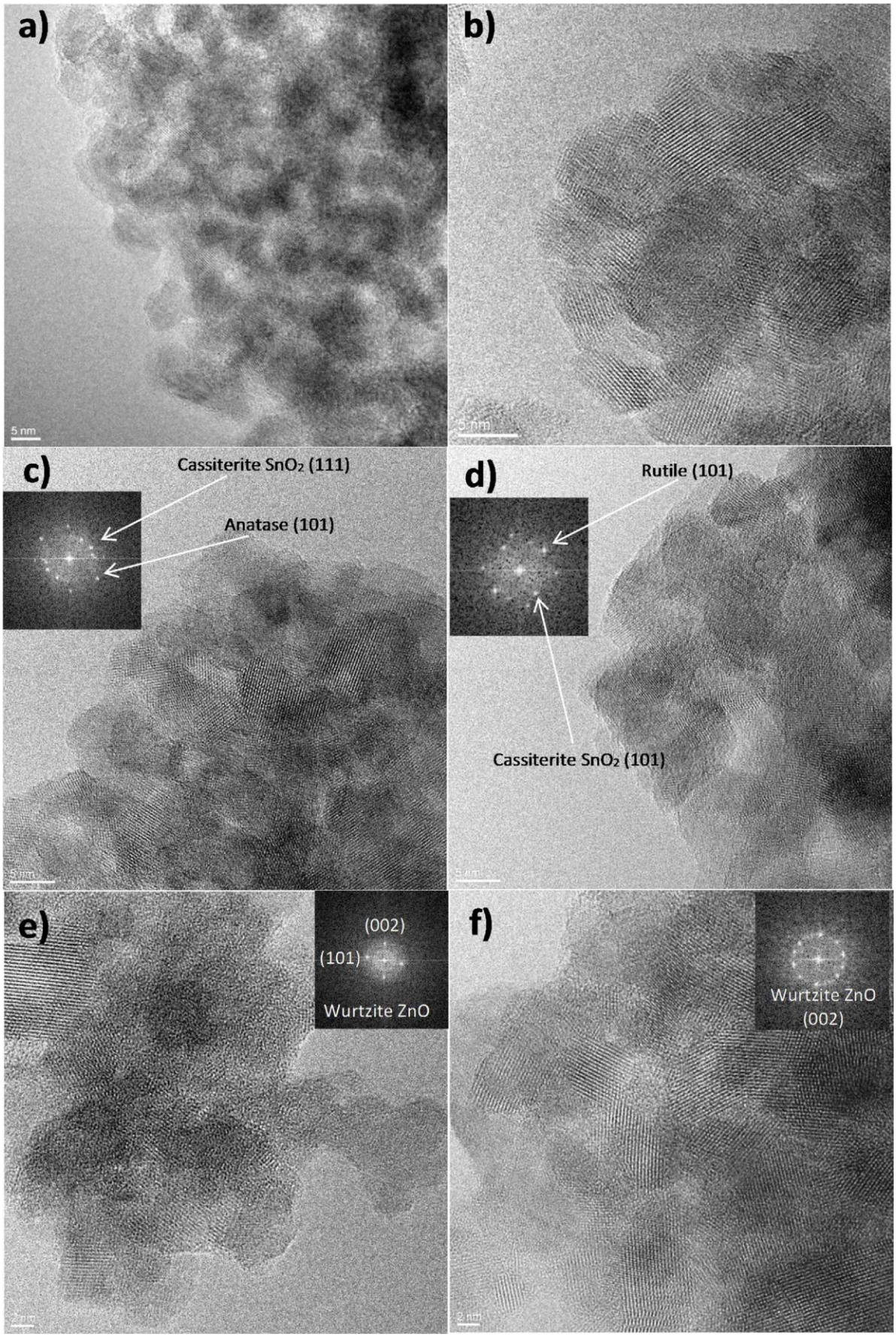
a)
5 nm
b)
5 nm
c)
Cassiterite SnO_2 (111)
Anatase (101)
5 nm
d)
Rutile (101)
Cassiterite SnO_2 (101)
5 nm
e)
(002)
(101)
Wurtzite ZnO
2 nm
f)
Wurtzite ZnO
(002)
2 nm

Figure 4

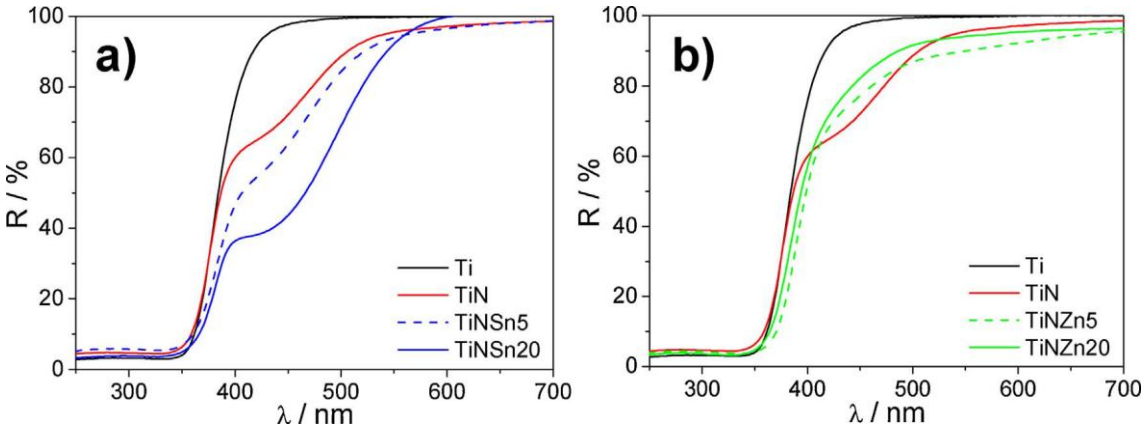

Figure 5